Front. Struct. Civ. Eng. 2023, 17(7): 981–993
https://doi.org/10.1007/s11709-023-0979-5

RESEARCH ARTICLE

Multi-harmonic forced vibration and resonance of simple beams to moving vehicles

Zhi SUN[a,b*], Limin SUN[a,b], Ye XIA[b]

[a] *State Key Laboratory for Disaster Reduction in Civil Engineering, Shanghai 200092, China*
[b] *Department of Bridge Engineering, Tongji University, Shanghai 200092, China*
[*] *Corresponding author. E-mail: sunzhi1@tongji.edu.cn*

ABSTRACT This study modeled the moving-vehicle-induced forcing excitation on a single-span prismatic bridge as a multiple frequency-multiplication harmonic load on the modal coordinates of a linear elastic simple Euler–Bernoulli beam, and investigated the forced modal oscillation and resonance behavior of this type of dynamic system. The forced modal responses consist of multiple frequency-multiplication steady-state harmonics and one damped mono-frequency complementary harmonic. The analysis revealed that a moving load induces high-harmonic forced resonance amplification when the moving speed is low. To verify the occurrence of high-harmonic forced resonance, numerical tests were conducted on single-span simple beams based on structural modeling using the finite element method (FEM) and a moving sprung-mass oscillator vehicle model. The forced resonance amplification characteristics of the fundamental mode for beam response estimation are presented with consideration to different end restraint conditions. The results reveal that the high-harmonic forced resonance may be significant for the investigated beams subjected to vehicle loads moving at specific low speeds. For the investigated single-span simple beams, the moving vehicle carriage heaving oscillation modulates the beam modal frequency, but does not induce notable variation of the modal oscillation harmonic structure for the cases that vehicle of small mass moves in low speed.

KEYWORDS forced vibration, linear Euler beam, moving load, harmonic structure, frequency modulation, end restraints

1 Introduction

The dynamic behavior of bridges and spanning structures during operation is the subject of ongoing research in the field of structural and infrastructure engineering. Most existing studies on this subject have focused on the free vibration behavior of structures. For beams with general boundary restraints, modal characteristic equations have been formulated, and the modal frequencies and mode shapes have been analyzed [1–3]. Under the different actions and mechanisms of interaction of the operation and environmental loads with bridges, structural vibrations exhibit various patterns. Therefore, it is important to understand the vibration behavior patterns and characteristics for bridge design and behavior manipulation.

Article history: Received Sep 16, 2022; Accepted Jan 14, 2023

Moving vehicle loads are the most common load type for bridges and traffic infrastructure. The excitation of different moving vehicle loads on the supporting structures may induce various resonances [4–16] and diverse spatial-temporal shapes and patterns [17–21] under different operation scenarios. If each moving vehicle load is simplified as a concentrated force, the governing equations in the modal domain will be uncoupled and the analytical solutions of the modal response can be derived. A classical analytical solution has been derived for a single-span simply supported uniform beam [22]. According to this derivation, when forced resonance occurs, the critical moving speed is equal to twice the beam span length divided by the period of the fundamental mode. Pesterev et al. [23] analytically derived the maximum response function for a simply supported beam and numerically constructed this function for a clamped–clamped beam based on the assumption

that the beam's maximum response can be approximated using the fundamental mode. Mamandi et al. [24] investigated the longitudinal–transverse nonlinear coupled dynamic behavior of an inclined uniform pinned–pinned beam under the simultaneous action of an axial force and transverse moving force with consideration to mid-plane stretching. Piccardo and Tubino [25] analyzed the amplitude modulation characteristics and maximum response of Euler–Bernoulli beams under resonant harmonic moving loads. Johansson et al. [26] derived a closed-form solution for the vibration of a multi-span beam under moving loads by solving the governing equation of motion in the frequency domain using Laplace transformation. Gašić et al. [27] conducted a study based on assumed modes with polynomial shape functions to approximately determine the dynamic response of a flexible L-shaped structure with a lumped tip mass subjected to a moving load. Tan et al. [28] analyzed the natural frequency and mode shapes of a continuous beam bridge under different vehicle loading conditions. Maximov and Dunchev [29] analytically investigated the dynamic response of a bridge crane to the telpher moving load based on the multi-harmonic interpolation of the structural deflection shape. Jeong et al. [30] analyzed the vibration of a multi-span beam subjected to a moving point force using the frequency domain spectral element method.

This study analytically investigated the moving-vehicle-induced multiple frequency-multiplication modal forced oscillation (MFMFO) behavior of supporting single-span Euler–Bernoulli beams with end rotation linear elastic restraints (ERLERs). A unified load model is proposed to represent the moving-load-induced forcing excitation on the modal coordinates as multiple frequency-multiplication harmonic forces. The forced resonance occurrence condition is discussed, and the closed-form modal oscillation and resonance responses are derived. Case studies were conducted using finite element method (FEM) structural modeling based on numerical integration to verify the analytical pattern and accuracy of the derived solution. Based on the analytical solutions, the modal oscillation amplitude magnification and phase angle characteristics for single-span generally supported simple beams were computed.

2 Formulation

2.1 System modeling

The investigated structure is a single-span beam with ERLER of length L and uniform cross-section, as shown in Fig. 1. The considered loads are the two-axle vehicle loads with an axle spacing of l_v in a series with a uniform spacing distance l_o traveling at constant speed s. Under the assumptions that the bridge conforms to the basic hypothesis of a linear elastic Euler–Bernoulli beam with Rayleigh damping and each vehicle load can be simplified as a moving sprung-mass oscillator to account for its heaving oscillation, the governing equations of motion (EOM) for the vertical vibration of the bridge and the vehicles are expressed as follows:

$$EI\frac{\partial^4 v(x,t)}{\partial x^4}+c_1EI\frac{\partial^3 v(x,t)}{\partial x^2\partial t}+\bar{m}\frac{\partial^2 v(x,t)}{\partial t^2}+c_0\bar{m}\frac{\partial v(x,t)}{\partial t}=\sum_{i=1}^{N_o}F_i\delta(x-st_i), \tag{1a}$$

$$m_v\ddot{q}_{v,i}+k_v\left[q_{v,i}-v(st_i,t)\right]=0, \tag{1b}$$

$$F_i=k_v\left[q_{v,i}-v(st_i,t)\right]+m_vg, \tag{1c}$$

where EI, $\bar{m}=\rho A$, c_0, c_1, and $v(x,t)$ denote the flexural rigidity, mass of the unit length, mass proportional Rayleigh damping factor, stiffness proportional Rayleigh damping factor, and vertical deformation of the beam bridge, respectively; $t_i=t-(i-1)\hat{T}$ $(\hat{T}=\frac{l_0}{s})$ denotes the traveling time of the ith moving force F_i on the beam bridge owing to the ith vehicle; δ is Dirac's delta function; x is the longitudinal coordinate of the beam bridge, which is counted from the origin at the left end-support of the beam bridge; m_v, k_v, and $q_{v,i}$ are the mass, stiffness, and vertical motion of the ith vehicle sprung mass oscillator, respectively; '$\cdot$' denotes differentiation with respect to time t; g is the gravitational acceleration. The associated boundary conditions of the beam are expressed as follows:

$$EI\frac{\partial^2 v(0,t)}{\partial x^2}=k_{\theta i}\frac{EI}{L}\frac{\partial v(0,t)}{\partial x},\quad v(0,t)=0, \tag{2a}$$

Fig. 1 Bridge consisting of single-span prismatic linear elastic Euler beam subjected to moving vehicle loads.

$$EI\frac{\partial^2 v(L,t)}{\partial x^2} = -k_{\theta j}\frac{EI}{L}\frac{\partial v(L,t)}{\partial x}, \qquad v(L,t) = 0, \tag{2b}$$

where $k_{\theta i}\dfrac{EI}{L}$ and $k_{\theta j}\dfrac{EI}{L}$ are the rotational spring constants at the left and right ends of the beam bridge, respectively. For simplicity, the cases wherein $l_0 = L$ are considered in the following derivation.

2.2 Beam eigen-mode analysis

To interpolate the beam response, the beam modal information ϕ_r and ω_r, that is, the mass-normalized mode shape and resonance frequency of the rth beam mode, are analyzed. The governing equation for the eigenmode analysis of the beam is expressed as follows.

The solution to Eq. (3) can be expressed as follows:

$$EI\frac{\mathrm{d}^4\phi_r(x)}{\mathrm{d}x^4} - \bar{m}\omega_r\phi_r(x) = 0, \tag{3a}$$

$$\frac{\mathrm{d}^2\phi_r(0)}{\mathrm{d}x^2} = \frac{k_{\theta i}}{L}\frac{\mathrm{d}\phi_r(0)}{\mathrm{d}x}, \qquad \phi_r(0) = 0, \tag{3b}$$

$$\frac{\mathrm{d}^2\phi_r(L)}{\mathrm{d}x^2} = -\frac{k_{\theta j}}{L}\frac{\mathrm{d}\phi_r(L)}{\mathrm{d}x}, \qquad \phi_r(L) = 0, \tag{3c}$$

$$\begin{aligned}\phi_r(x) = {} & C_{1,r}\sin[(\lambda_r L)\bar{x}] + C_{2,r}\cos[(\lambda_r L)\bar{x}] \\ & + C_{3,r}\sinh[(\lambda_r L)\bar{x}] + C_{4,r}\cosh[(\lambda_r L)\bar{x}],\end{aligned} \tag{4}$$

where $\bar{x} = \dfrac{x}{L}$, $C_{1,r}$, $C_{2,r}$, $C_{3,r}$, and $C_{4,r}$ are constants determined from the boundary conditions using the following equations:

$$\begin{bmatrix} k_{\theta i} & \lambda_r L & k_{\theta i} & -\lambda_r L \\ 0 & 1 & 0 & 1 \\ \begin{pmatrix} k_{\theta j}\cos(\lambda_r L) \\ -\lambda_r L\sin(\lambda_r L) \end{pmatrix} & \begin{pmatrix} -k_{\theta j}\sin(\lambda_r L) \\ -\lambda_r L\cos(\lambda_r L) \end{pmatrix} & \begin{matrix} k_{\theta j}\cosh(\lambda_r L) \\ +\lambda_r L\sinh(\lambda_r L) \end{matrix} & \begin{pmatrix} k_{\theta j}\sinh(\lambda_r L) \\ +\lambda_r L\cosh(\lambda_r L) \end{pmatrix} \\ \sin(\lambda_r L) & \cos(\lambda_r L) & \sinh(\lambda_r L) & \cosh(\lambda_r L) \end{bmatrix} \begin{bmatrix} C_{1,r} \\ C_{2,r} \\ C_{3,r} \\ C_{4,r} \end{bmatrix} = 0, \tag{5}$$

and $\lambda_r L = \sqrt[4]{\dfrac{\bar{m}\omega_r^2}{EI}}$ is the frequency parameter. To obtain a nontrivial solution, the determinant of the coefficient matrix of the above equations must be set to zero.

Because the investigated beams have rigid displacement restraints at both ends, the mode shape function $\phi_r(x)$ can be considered as one cycle of a periodic continuous function, which can be expressed as the following Fourier series:

$$\phi_r x = a_{0,r} + \sum\nolimits_{n=1}^{\infty} a_{n,r}\cos\frac{2n\pi x}{L} + \sum\nolimits_{n=1}^{\infty} b_{n,r}\sin\frac{2n\pi x}{L}, \tag{6}$$

where $a_{0,r}$, $a_{n,r}$, and $b_{n,r}$ are the Fourier coefficients expressed using $C_{1,r}$, $C_{2,r}$, $C_{3,r}$, $C_{4,r}$, and $(\lambda L)_r$, as follows:

$$a_{0,r} = \frac{2C_{1,r}\sin^2\dfrac{\lambda_r L}{2} + C_{2,r}\sin(\lambda_r L) + 2C_{3,r}\sinh^2\dfrac{\lambda_r L}{2} + C_{4,r}\sinh(\lambda_r L)}{\lambda_r L}, \tag{7a}$$

$$a_{n,r} = 2\lambda_r L\left[\frac{C_{1,r}\cos(\lambda_r L) - C_{1,r} - C_{2,r}\sin(\lambda_r L)}{4n^2\pi^2 - (\lambda_r L)^2} + \frac{2C_{3,r}\sinh^2\dfrac{\lambda_r L}{2} + C_{4,r}\sinh(\lambda_r L)}{4n^2\pi^2 + (\lambda_r L)^2}\right], \tag{7b}$$

$$b_{n,r} = -4n\pi\left[\frac{C_{1,r}\sin(\lambda_r L) + C_{2,r}\cos(\lambda_r L) - C_{2,r}}{4n^2\pi^2 - (\lambda_r L)^2} + \frac{C_{3,r}\sinh(\lambda_r L) + 2C_{4,r}\sinh^2\dfrac{\lambda_r L}{2}}{4n^2\pi^2 + (\lambda_r L)^2}\right]. \tag{7c}$$

Please see Appendix A for further details.

2.3 Forced vibration analysis

By expressing the structural vibration at any instant using the modal coordinates, the EOM can be transformed into uncoupled ordinary differential equations to compute the modal response using the Galerkin method. For the rth

modal coordinate, the governing equation of motion is expressed as follows:

$$M_r\ddot{v}_r(t)+C_r\dot{v}_r(t)+K_r v_r(t)=F\phi_r(st), \tag{8}$$

where $v_r(t)$ is the response of the rth mode; M_r, C_r, and K_r are the modal mass, damping, and stiffness coefficient expressed as $M_r=M_\mathrm{b}$, $C_r=2M_r\xi_r\omega_r$, $K_r=M_r\omega_r^2$; $M_\mathrm{b}=\int_0^L\bar{m}(x)\mathrm{d}x$; $\xi_r=\dfrac{c_0}{2\omega_r+\dfrac{c_1\omega_r}{2}}$ is the proportional damping ratio of the rth mode. As can be seen, if the vehicle heaving oscillation acceleration is controlled to be significantly smaller than the vehicle gravity force $m_\mathrm{v}g$, the main oscillation response component of the beam modal coordinates can be considered as the response under a moving concentrated force with magnitude $m_\mathrm{v}g$. The term on the right-hand side of Eq. (8) can now be treated as multiple frequency-multiplication harmonic excitations on the modal coordinates; multiple forced resonances will occur when $\omega=\dfrac{2\pi s}{L}$ approaches $\dfrac{\omega_r}{n}$ for each mode.

If the beam is considered to be in static initially, the modal oscillation can be obtained according to Duhamel's integral, as follows:

$$v_r(t)=\frac{1}{M_r\omega_r^\mathrm{D}}\int_0^t F\phi_r(s\tau)\mathrm{e}^{-\xi_r\omega_r(t-\tau)}\sin\left[\omega_r^\mathrm{D}(t-\tau)\right]\mathrm{d}\tau, \tag{9}$$

where $\omega_r^\mathrm{D}=\omega_r\sqrt{1-\xi_r^2}$ is the damped frequency of the rth mode. By substituting Eq. (6) into Eq. (9), the modal response can be further expressed in the following form with multiple frequency-multiplication forced steady-state response components and a mono-frequency transient response component, as follows:

$$\begin{aligned}v_r(t)=&\frac{Fp_{\phi_r}}{K_r}\sum\nolimits_n\rho_{n,r}\sin(n\bar{\omega}t+\psi_{n,r})\\&+A_{\mathrm{c},r}\sin(\omega_r^\mathrm{D}t+\psi_{c,r})\exp(-\xi_r\omega_r t),\end{aligned} \tag{10}$$

where $p_{\phi_r}=\max(\phi_r(x))$,

$$\rho_{n,r}=\frac{A_{n,r}}{p_{\phi_r}\sqrt{\left(1-\left(n\dfrac{\beta}{\beta_r}\right)^2\right)^2+\left(2n\xi_r\dfrac{\beta}{\beta_r}\right)^2}}, \tag{11a}$$

$$\psi_{n,r}=\theta_{n,r}-\arctan\left(2n\xi_r\frac{\beta}{\beta_r},\left(1-n^2\frac{\beta^2}{\beta_r^2}\right)\right), \tag{11b}$$

where $A_{n,r}=\sqrt{a_{n,r}^2+b_{n,r}^2}$, $\theta_{n,r}=\arctan(a_{n,r},\ b_{n,r})$, $\beta=\dfrac{\bar{\omega}}{\omega_\mathrm{b}}$, $\beta_r=\dfrac{\omega_r}{\omega_\mathrm{b}}$, $\omega_\mathrm{b}=\omega_1$, $A_{\mathrm{c},r}$, and $\psi_{\mathrm{c},r}$ are constants determined from the given initial conditions of the modal coordinates $v_r(0)$ and $\dot{v}_r(0)$. Specifically, under the undamped condition, the forced modal resonance response when $\bar{\omega}=\dfrac{\omega_r}{l}$ can be expressed as follows:

$$\begin{aligned}v_r(t)=&\frac{Fp_{\phi_r}}{K_r}\sum\nolimits_n^{n\neq l}\rho_{n,r}\sin(n\bar{\omega}t+\psi_{n,r})\\&-\frac{FA_{l,r}}{2K_r}\omega_r t\cos(\omega_r t+\psi_{l,r})+A_{\mathrm{c},r}\sin(\omega_r t+\psi_{c,r}).\end{aligned} \tag{12}$$

Then, the structural displacement response can be calculated by mode summation, as follows:

$$v(x,t)=\sum\nolimits_r\phi_r(x)v_r(t). \tag{13}$$

By differentiating Eq. (13) with respect to time, the structural velocity and acceleration responses can be calculated.

3 Case studies

According to the proposed theoretical model and derived analytical solutions, the following computations were carried out to verify the proposed method and analyze the MFMFO amplitude magnification and phase angle characteristics.

3.1 Modal characteristics

For a single-span beam with arbitrary ERLER stiffness, the modal frequency parameters and mode shape coefficients were first determined. Figure 2 shows the frequency parameters computed for the first two modes when $k_{\theta i}$ and $k_{\theta j}$ vary in the range of 10^{-5}–10^{7}. As can be seen, the distributions computed for both modes are symmetric about line $k_{\theta i}=k_{\theta j}$, and consist of four platforms and in-between transition regions. These four

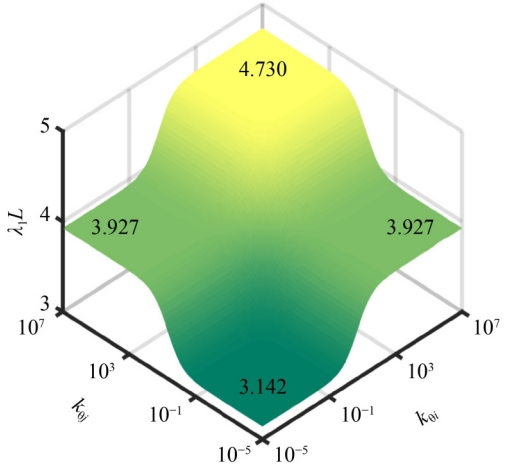

Fig. 2 Computed frequency parameters ($\lambda_r L$) for fundamental mode of bridge consisting of single-span beam with varying end rotation linear elastic stiffness.

platforms correspond to four case classes with the idealized end restraints. For the platform with $\lambda_1 L = 3.142$ and $\lambda_2 L = 6.283$, the corresponding boundary conditions can be approximated as a hinged–hinged restraint. For the platform with $\lambda_1 L = 3.927$ and $\lambda_2 L = 7.069$, the corresponding boundary conditions can be approximated as clamped–hinged or hinged–clamped restraints. For the platform with $\lambda_1 L = 4.730$ and $\lambda_2 L = 7.853$, the corresponding boundary conditions can be approximated as clamped–clamped restraints. As shown in Fig. 3, the mode shape parameter distributions computed for the first two modes also consist of four platforms and in-between transition regions.

Subsequently, the magnitudes and phase angles of the mode-shaped Fourier series multi-harmonic components were computed. Figures 4 and 5 show the results for the first four Fourier series components of the fundamental mode. As can be seen, for this mode, the 0th expansion term, which is a constant term, and the 1st harmonic component are the most important. The presented high-harmonic magnitudes exhibit a monotonically decreasing trend. For higher modes, as the number of inflection points increases, some high-harmonic components become more important for the composition of the corresponding mode shapes. For example, for the second mode, because there is one point of inflection in the related mode shape, the 1st harmonic is the most important.

3.2 Verification of analytical solution

To verify the analytical solution, numerical tests based on FEM structural modeling were conducted for cases wherein $k_{\theta i} = k_{\theta j} = 10^{-5}$, $\xi_1 = \xi_2 = 0\%$. The bridge was modeled using 20 2-node 4-degree of freedom (DOF) Euler–Bernoulli beam elements to account for the stiffness of the ERLERs. The considered sprung-mass vehicle oscillator has mass $m_v = 0.1 M_b$ and frequency $\omega_v = 0.23\omega_b$. The initial displacement, velocity, and acceleration of each sprung-mass oscillator are set to zero when the oscillator enters the beam. The force vector at each step is updated according to the magnitude and on-element location of the load. The Newmark method was used to compute the dimensionless displacement and velocity responses, which are defined as follows for the given end constraints:

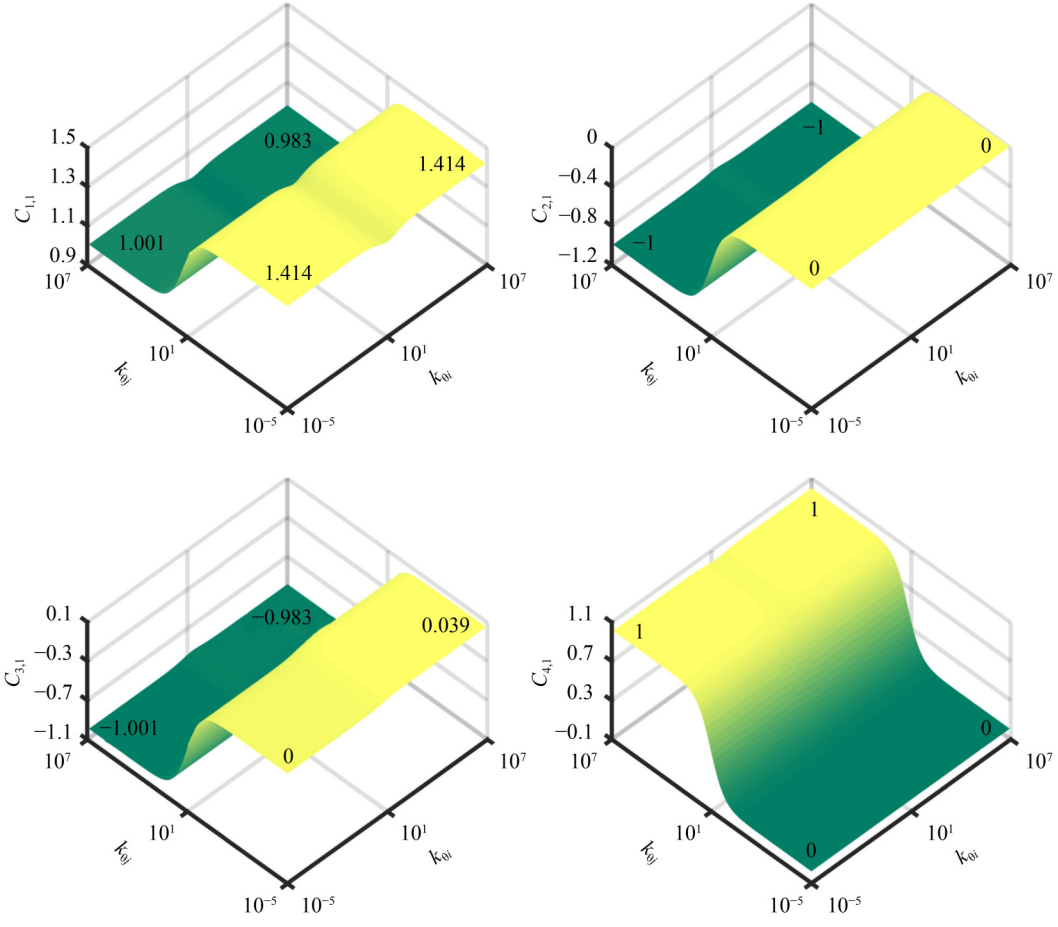

Fig. 3 Computed mode shape parameters for fundamental mode of bridge consisting of single-span beam with varying end rotation linear elastic stiffness.

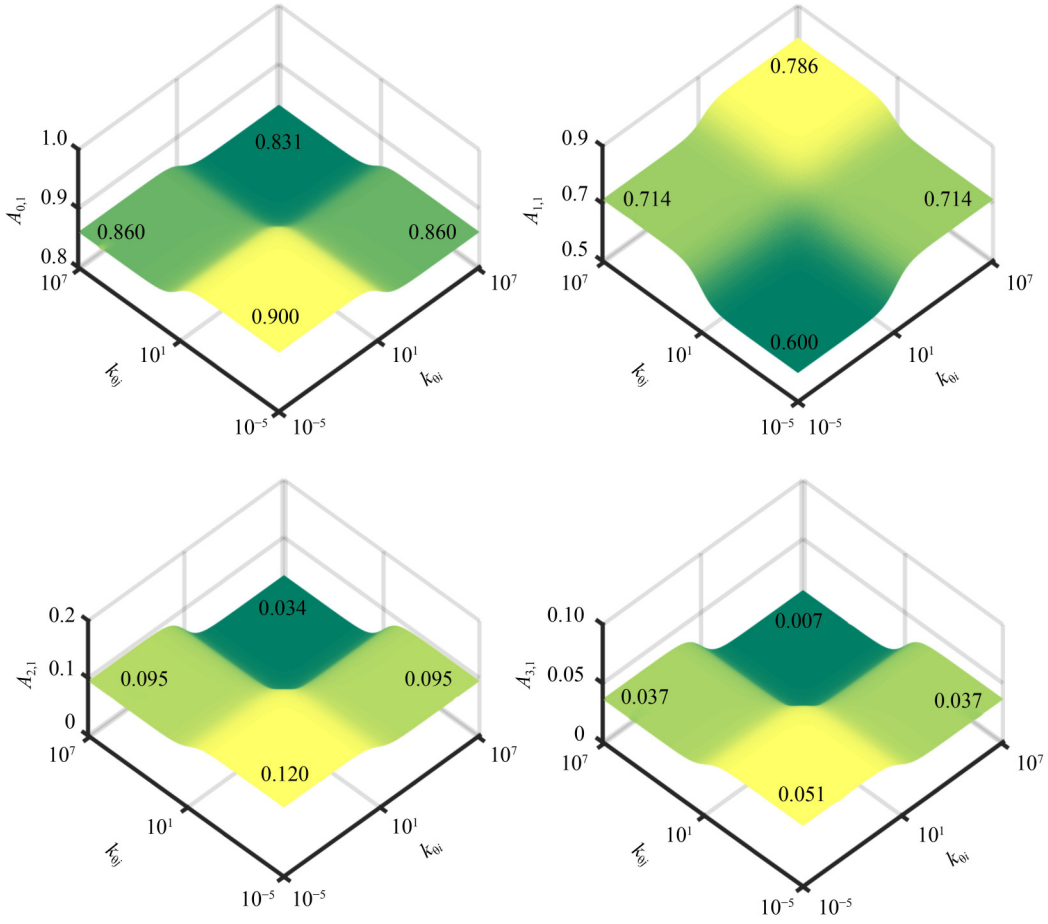

Fig. 4 Magnitude of multi-harmonic components for fundamental mode shape of bridge consisting of single-span beam with varying end rotation linear elastic stiffness.

$$\bar{v} = \frac{48EI}{FL^3} v,$$

$$\dot{\bar{v}} = \frac{48EI}{FL^3\omega_1} \dot{v}. \tag{14}$$

Based on the MFMFO moving load model, the dynamic amplification and phase angle curves for the first nine forced oscillation components ($n = 0$–8) of the fundamental mode of the single-span beam bridge with $k_{\theta i} = k_{\theta j} = 10^{-5}$ and $\xi_1 = 1\%$ were computed as shown in Fig. 6. As can be seen, the importance of frequency-multiplication harmonic oscillations decreases as n increases. Around the resonance peak of each high-harmonic component, the amplification and in-phase to out-of-phase transition of the related harmonic oscillation will give rise to the secondary oscillation of modal responses, as shown in Figs. 7 and 8.

Figure 7 shows the analytical solutions computed for the MFMFO model and the moving oscillator numerical integration results obtained for the FEM model when $\beta = 0.3$. As can be seen, there is good agreement between the dimensionless displacement and velocity responses in the $5T$ durations (where $T = \frac{L}{s}$) of the physical and modal coordinates in the MFMFO model analytical derivation and FEM model numerical integration results. The amplitude spectra, which are shown relative to the dimensionless frequency $\Omega = \frac{\Omega}{\bar{\Omega}}$, of the $\bar{v}$ responses confirm the accuracy of the analytical solution of the MFMFO model, and are in good agreement with the numerical integration results of the FEM model. Moreover, the amplitude spectrum indicates that the structural modal oscillation of the fundamental mode consists of multiple frequency-multiplication components at $\Omega = n$, which are the forced oscillations of this mode, and one component at $\Omega = \frac{1}{\beta} = 3.3$, which corresponds to the complementary oscillation of this mode. For the second mode, the amplitude spectrum reveals that the structural modal oscillation for this mode consists of one component at $\Omega = 1$ and one component at $\Omega = 13.3$. Considering that the mode shape parameters have only one nonzero term ($b_{1,2}$) for the second mode when $k_{\theta i} = k_{\theta j} = 10^{-5}$, the forced oscillation in this case,

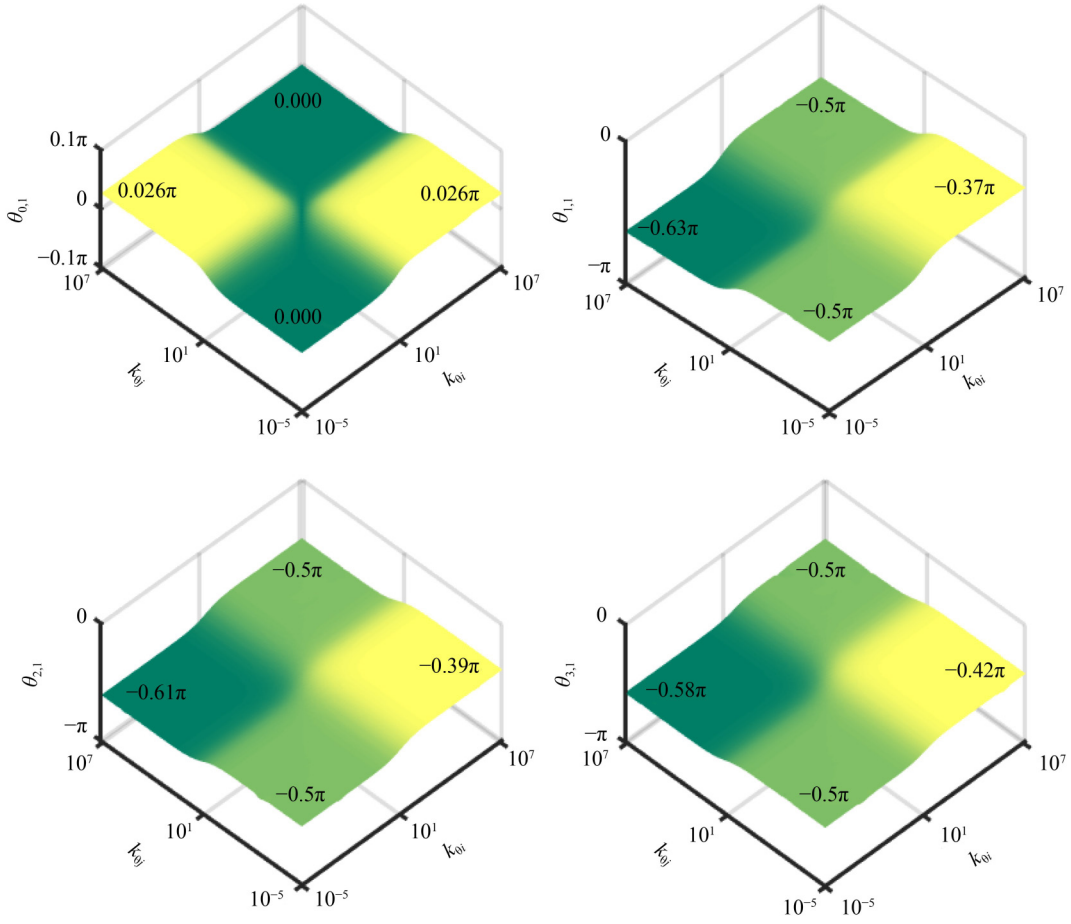

Fig. 5 Phase angle of multi-harmonic components for fundamental mode shape of bridge consisting of single-span beam with varying end rotation linear elastic stiffness.

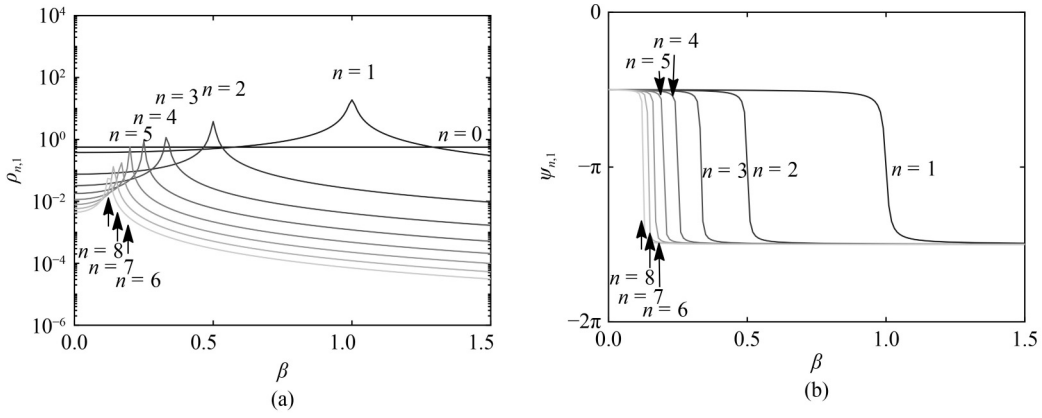

Fig. 6 Multi-harmonic dynamic amplification: (a) phase angle; (b) curves computed for fundamental mode of bridge consisting of single-span beam with $k_{\theta i} = k_{\theta j} = 10^{-5}$, $\xi_1 = 1\%$.

including one harmonic at $n = 1$, is reasonable. For the component at $\Omega = 13.3$, because $\Omega_2 = 4\Omega_1$ when $k_{\theta i} = k_{\theta j} = 10^{-5}$, this component is the second-mode complementary oscillation, according to the derived analytical solution.

To verify the undamped resonance solution, Fig. 8 shows the analytical solutions obtained for the MFMFO moving load model and the numerical integration results obtained for the FEM moving oscillator model when $\beta = 0.33$ or $s = \dfrac{\omega_1 L}{6\pi}$. As can be seen, the dimensionless displacement and velocity responses of the cross section at $x = 0.4L$ and those of the first two modes obtained from both methods are in good agreement. At $\beta = 0.33$, the resonance of the third and complementary

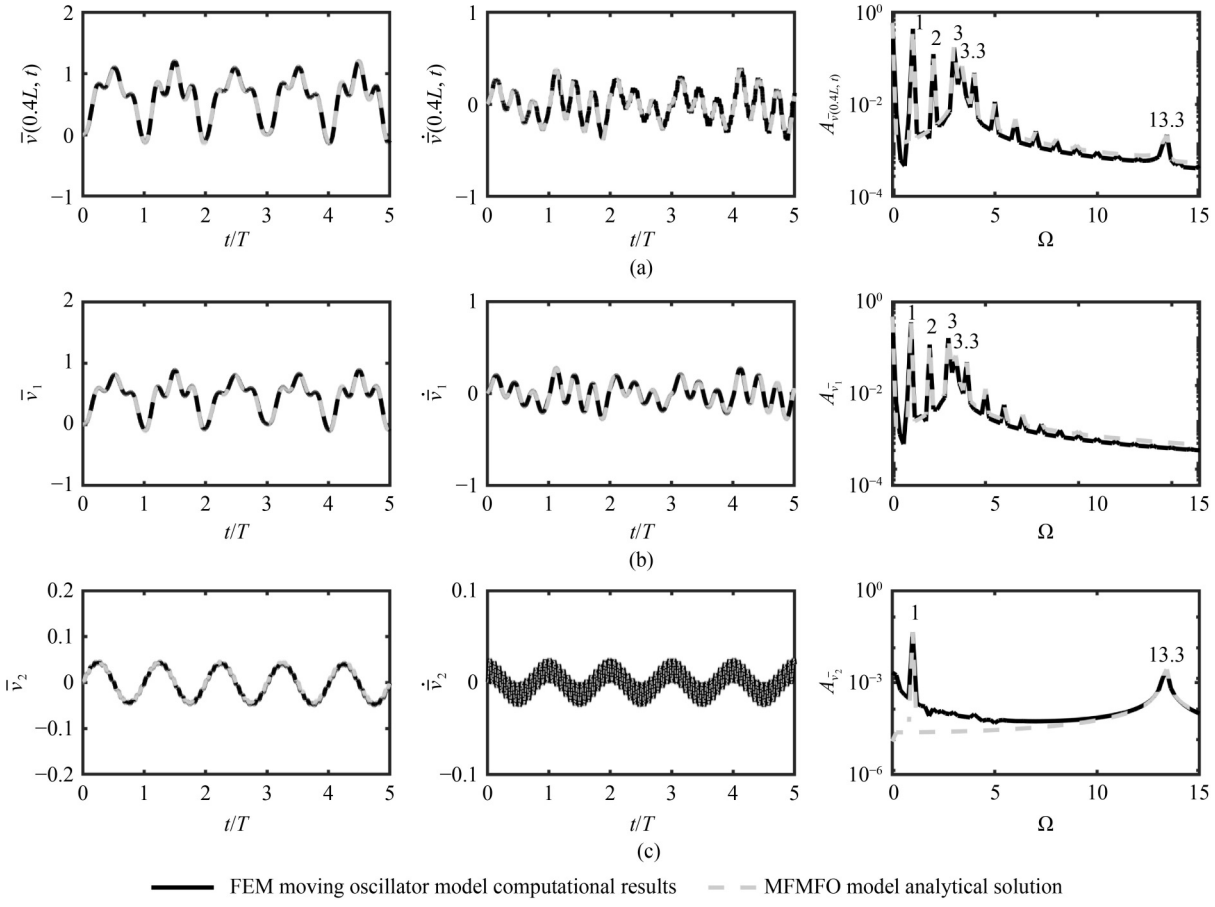

Fig. 7 Moving-load-induced forced non-resonance vibration displacement and velocity responses of structure, and amplitude spectrum of: (a) cross-section at $x = 0.4L$; (b) mode 1; (c) mode 2 for bridge consisting of single-span beam with $k_{\theta i} = k_{\theta j} = 10^{-5}$, $\beta = 0.3$, $\xi_1 = \xi_2 = 0\%$, obtained by numerical integration of FEM moving oscillator model and analytical solution of MFMFO model.

components of the fundamental mode occurs. The forced resonance divergent oscillation is so powerful that the structural displacement and velocity response are significantly amplified just after five cycles, although $A_{3,1}$ is quite small, as shown in Fig. 4. The amplitude spectra also indicate the occurrence of this resonance in the fundamental mode, with a main peak at $\Omega = 3$. Considering the single-frequency forced oscillation pattern, the second mode does not exhibit a divergent time-domain oscillation shape. The amplitude spectrum shows that the modal oscillation of this mode consists of one component at $\Omega = 1$ and one component at $\Omega = \dfrac{\beta_2}{\beta} = 12$.

3.3 Damped resonance amplification characteristics

Based on the verified analytical solution, the MFMFO dynamic amplification and phase angle characteristics of the multiple modulated-harmonic modal forced resonance oscillations were computed using Eqs. (11a) and (11b) for single-span beams with varying end-rotational restraints. In this paper, only cases with $\xi = 1\%$ are presented. For the 0th modal forcing excitation, which is actually a step excitation, magnitude amplification does not occur because the forced response is also a step function with the magnitude of the corresponding static response. For non-constant oscillating excitations, forced resonance occurs in different frequency regions and may induce significant magnitude amplifications for the damped steady-state response under multiple periods of forcing excitation.

Figure 9 shows the peak resonance amplifications with consideration to the high-harmonic forcing excitation on the fundamental mode when $\xi = 1\%$. For this mode, the first modulated-harmonic forced resonance is the most important among the multiple forced resonances. The corresponding $\rho_{1,1}$ value varies from 19.89 for the hinged–hinged restraints to 24.75 for the clamped–clamped restraints. For the high-harmonic forced resonances, $\rho_{n,1}$ monotonically decreases as n increases from 1 to 4 for any given pair of $k_{\theta i}$ and $k_{\theta j}$. When $n = 4$, $\rho_{4,1}$ is always below 1 and varies from 0.066 for the clamped–clamped restraints to 0.947 for the hinged–hinged restraints. For the higher modes, the high-harmonic component is the

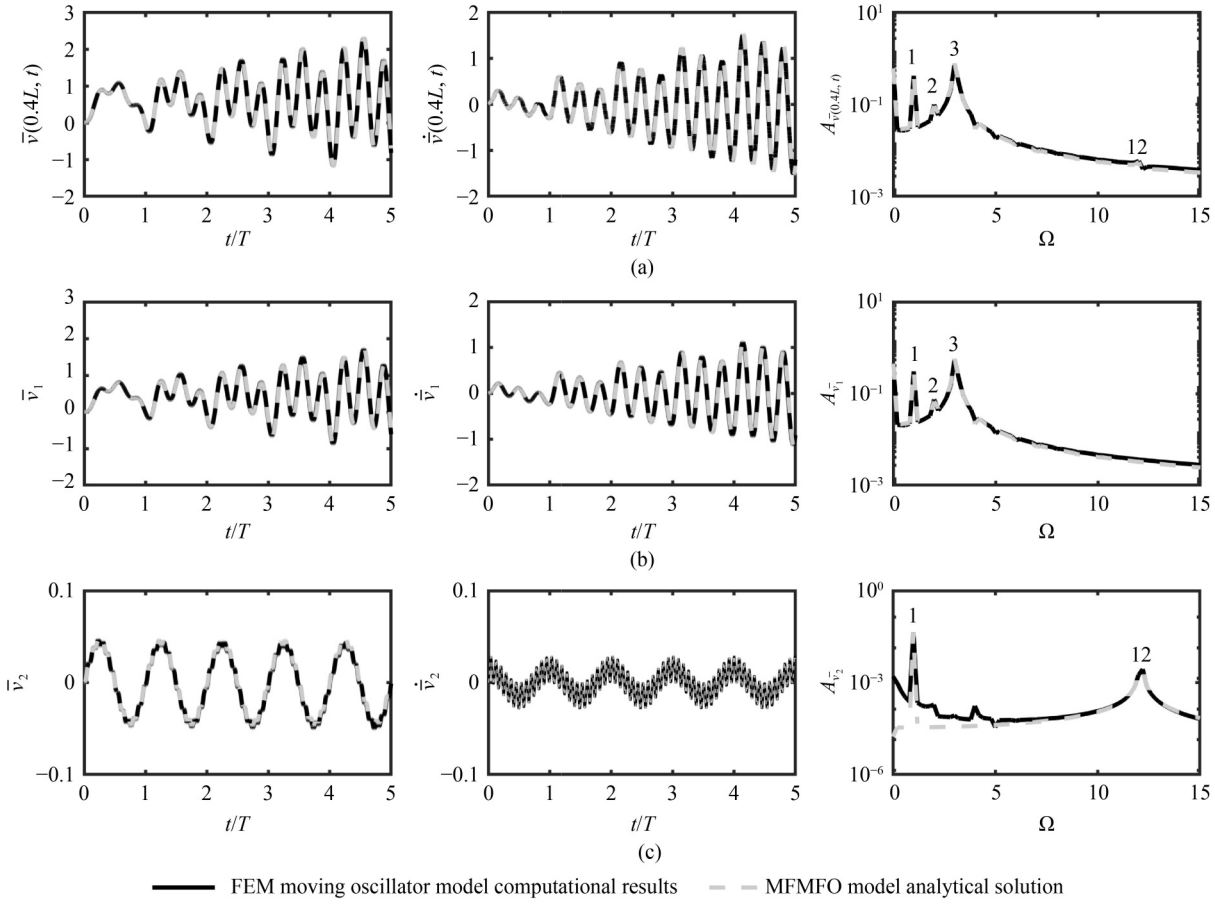

Fig. 8 Moving-load-induced forced resonance displacement and velocity responses of structure, and amplitude spectrum of: (a) cross-section at $x = 0.4L$; (b) mode 1; (c) mode 2 for bridge consisting of single-span beam with $k_{\theta i} = k_{\theta j} = 10^{-5}$, $\beta = 0.33$, $\xi_1 = \xi_2 = 0\%$, obtained by numerical integration of FEM moving oscillator model and analytical solution of MFMFO model.

primary harmonic of the excitation. Although the low participation of the higher modes may diminish the unfavorable dynamic loading effect, the high-harmonic resonance amplification must be checked to ensure the safety of the stress and stress resultant in the loading period of one moving vehicle.

3.4 Vehicle heaving and frequency modulation

Obviously, vehicle oscillation may induce harmonic structure variation and additional frequency and amplitude modulations in the modal oscillation response of the supporting beam. This study investigated the vehicle carriage heaving oscillation effects based on structural modeling using FEM and numerical integration under a moving sprung-mass oscillator load. Because the forced high-harmonic resonance oscillation in the low-speed range has the most important theoretical and application value, the numerical cases around $\beta = 0.33$ were simulated for the investigated single-span supporting beam of $k_{\theta i} = k_{\theta j} = 10^{-5}$ under five periods of moving vehicle oscillator excitation.

To check the effective range of the derived harmonic structure with consideration to the vehicle heaving oscillation effect, the multi-harmonic function expressed by Eq. (12) was used as the baseline function to fit the numerically computed fundamental mode response obtained by the FEM structural model based on numerical integration for the initially resting beam subjected to a moving sprung-mass oscillator load in the range of $m_v \in [0.01, 0.30]\, m_b$ and $\omega_v \in [0.02, 1.00]\, \omega_b$. Five MFMFO components ($n = 0$–4) and one modal complementary oscillation component were considered in the curve-fitting baseline function. The amplitude, frequency, and phase angle of these oscillation components were set as the curve-fitting parameters. For the fitting of the oscillation response curve, it is much more important to set the initial value of the oscillation frequencies than to set the oscillation amplitude and phase angle. In this study, the optimizations from the driving frequency and beam fundamental modal frequency exhibit quick convergence, although vehicle heaving will induce the modulation of modal frequencies. Figure 10 shows the surface and contour plots of the

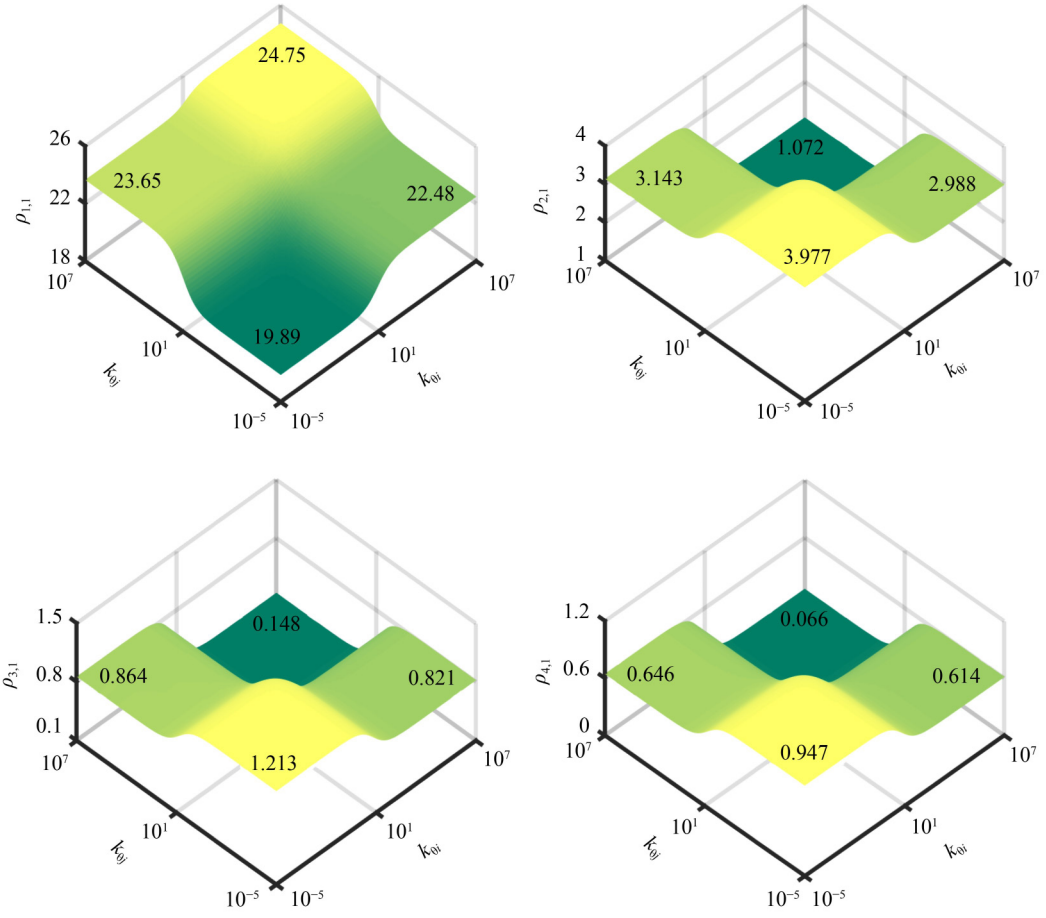

Fig. 9 Peak resonance amplification characteristics of moving-load forced *n*th (n = 1, 2, 3, 4) multi-harmonic oscillations for fundamental mode of bridge consisting of single-span beam with varying end rotation linear elastic stiffness when ξ_1 = 1%.

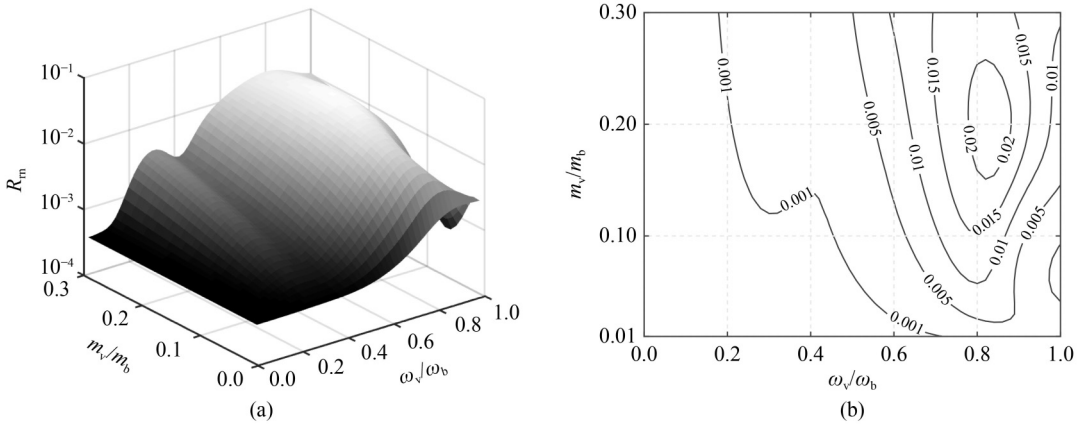

Fig. 10 (a) Surface; (b) contour plots of relative squared 2-norm residual for fitting of curve of numerically computed fundamental mode oscillation response of bridge, with consideration to vehicle heaving oscillation by using derived MFMFO function ($k_{\theta i} = k_{\theta j} = 10^{-5}$, $\beta = 0.33$, $\xi_1 = 0\%$).

relative squared 2-norm residual R_{rn}, which is defined as follows:

$$R_{\mathrm{rn}} = \frac{\mathrm{sum}\left[\left(v_{1,\mathrm{FEM}} - \tilde{v}_{1,\mathrm{MFMFO}}\right)^2\right]}{\mathrm{sum}\left(v_{1,\mathrm{FEM}}{}^2\right)}, \tag{15}$$

where $v_{1,\mathrm{FEM}}$ and $\tilde{v}_{1,\mathrm{MFMFO}}$ are the beam fundamental mode responses, as computed by the numerical integration of the FEM model under a moving sprung-mass and obtained by fitting the curve of the MFMFO oscillation structure. If the threshold of R_{rn} is set to 1%, the contour curve of 10^{-2} (Fig. 10) profiles the applicable range of the

derived MFMFO oscillation structure with consideration to the vehicle heaving oscillation perturbation. For convenience, the applicable condition can be conservatively set to $m_v \leqslant 0.30 m_b$ and $\omega_v \leqslant 0.60 \omega_b$.

The above-mentioned oscillation response curve fitting process can also be used to track the frequency modulation caused by the vehicle heaving oscillation, and detect abnormal operation scenarios. Figure 11 summarizes the fundamental modal frequency modulation factors β_b obtained from the above-mentioned oscillation response curve fitting optimization process with variation in the vehicle mass m_v and vehicle frequency ω_v within the applicable range. As can be seen, the fundamental mode frequency $\tilde{\omega}_b = \beta_b \omega_b$ of the modulated beam exhibits a smooth monotonically increasing trend in the observed region. The peak modal frequency shift ratio caused by this modulation is 5.6%. Considering the shape of the scatter distribution, the following frequency modulation factor function can be obtained by curve fitting to capture this trend for the considered approximately hinged–hinged simple beam.

$$\beta_b = 1.00 + 0.57 \frac{m_v}{m_b} \left(\frac{\omega_v}{\omega_b} \right)^2. \tag{16}$$

For this fit, the relative ratio of the squared 2-norm of the residual is 0.037%. The modulated modal frequency can be used to estimate the modal response of the beam under moving vehicle loads, with consideration to the carriage heaving oscillation of the investigated beam.

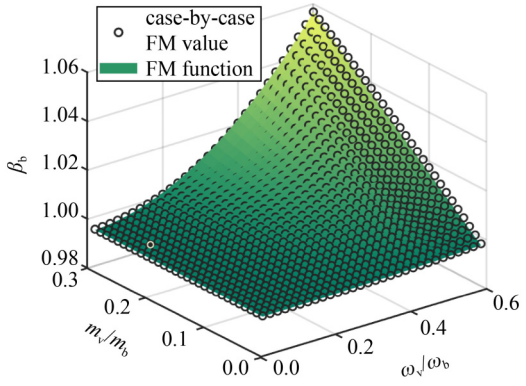

Fig. 11 Fundamental mode frequency modulation (FM) of bridge with consideration to vehicle heaving oscillation when $k_{\theta i} = k_{\theta j} = 10^{-5}$, $\beta = 0.33$, $\xi_1 = 0\%$.

4 Conclusions

Under the assumptions of the axle spacing of the vehicles being far shorter than the beam span and the vehicle carriage oscillation acceleration being far smaller than the gravitational acceleration, this study interpreted the moving-load-induced forcing excitation on the modal coordinates as multiple frequency-multiplication harmonic forces, and analytically investigated the modal forced oscillation characteristics for a supporting single-span linear Euler–Bernoulli simple beam. Closed-form modal forced non-resonance and resonance oscillations under moving forces were derived. As a baseline for comparison, structural modeling using FEM based on numerical integration was conducted under a moving oscillator. The applicable range of the derived MFMFO structure with consideration to the vehicle-heaving oscillation effect was computationally profiled. The following results were obtained for the considered beam.

• The moving-load-induced forced modal oscillations of the beam structure are generally considered to consist of multiple frequency-multiplication steady-state oscillations and one mono-frequency complementary oscillation.

• The multiple frequency-multiplication pattern of the modal forced oscillation results in forced resonance when the nth high-harmonic forcing frequency $n\omega$ approaches ω_r for the rth mode.

• The fundamental harmonic of the forced modal oscillation of the fundamental mode is the most important oscillation for the investigated category of single-span beams under the given moving load types.

• The derived MFMFO structure is effective within a wide region of relatively small vehicle mass and frequency with consideration to the vehicle carriage heaving oscillation. For the investigated beam, moving vehicle carriage heaving increased the fundamental frequency by up to 5.6% in pattern-reservation cases.

High-harmonic resonances may induce significant impact amplification and offset the peak response of the resultant stress envelope during the vehicle passage process [31]. When the beam shortening or stretching nonlinearity of the bridge, pitching, and other types of vehicle oscillation are considered, the vibration of beam bridges under moving vehicle loads exhibits more interesting spatial-temporal patterns, particularly in modal fission and fusion scenarios. Related studies will benefit bridge design and fatigue monitoring for engineering applications.

Appendix A: Derivation of Eqs. (7a)–(7c)

Based on Eqs. (4) and (6), the Fourier coefficients can be derived as follows.

$$\begin{aligned} a_{0,r} &= \frac{1}{L} \int_0^L \phi_r(x) \mathrm{d}x \\ &= \frac{1}{L} \int_0^L (C_1 \sin \lambda x + C_2 \cos \lambda x + C_3 \sinh \lambda x + C_4 \cosh \lambda x) \mathrm{d}x \\ &= \frac{2C_1 \sin^2 \frac{\lambda L}{2} + C_2 \sin \lambda L + 2C_3 \sinh^2 \frac{\lambda L}{2} + C_4 \sinh \lambda L}{\lambda L}, \end{aligned} \tag{A1}$$

$$
\begin{aligned}
a_{n,r} &= \frac{2}{L}\int_0^L \phi_r(x)\cos\frac{2n\pi x}{L}\mathrm{d}x = \frac{2}{L}\int_0^L (C_1\sin(\lambda x)+C_2\cos(\lambda x)+C_3\sinh(\lambda x)+C_4\cosh(\lambda x))\cos\frac{2n\pi x}{L}\mathrm{d}x \\
&= \frac{2}{L}\int_0^L C_1\sin(\lambda x)\cos\frac{2n\pi x}{L}\mathrm{d}x + \frac{2}{L}\int_0^L C_2\cos(\lambda x)\sin\frac{2n\pi x}{L}\mathrm{d}x + \frac{2}{L}\int_0^L C_3\sinh(\lambda x)\cos\frac{2n\pi x}{L}\mathrm{d}x \\
&\quad + \frac{2}{L}\int_0^L C_4\cosh(\lambda x)\cos\frac{2n\pi x}{L}\mathrm{d}x = \frac{2C_1}{L}\left[-\frac{\cos\left(\lambda+\frac{2n\pi}{L}\right)x}{2\left(\lambda+\frac{2n\pi}{L}\right)} - \frac{\cos\left(\lambda-\frac{2n\pi}{L}\right)x}{2\left(\lambda-\frac{2n\pi}{L}\right)}\right]_0^L \\
&\quad + \frac{2C_2}{L}\left[\frac{\sin\left(\lambda+\frac{2n\pi}{L}\right)x}{2\left(\lambda+\frac{2n\pi}{L}\right)} + \frac{\sin\left(\lambda-\frac{2n\pi}{L}\right)x}{2\left(\lambda-\frac{2n\pi}{L}\right)}\right]_0^L + \frac{2C_3}{L}\left[\frac{\lambda\cosh(\lambda x)\cos\frac{2n\pi x}{L}}{\lambda^2+\left(\frac{2n\pi}{L}\right)^2} + \frac{\frac{2n\pi}{L}\sinh(\lambda x)\sin\frac{2n\pi x}{L}}{\lambda^2+\left(\frac{2n\pi}{L}\right)^2}\right]_0^L \\
&\quad + \frac{2C_4}{L}\left[\frac{\lambda\sinh(\lambda x)\cos\frac{2n\pi x}{L}}{\lambda^2+\left(\frac{2n\pi}{L}\right)^2} + \frac{\frac{2n\pi}{L}\cosh(\lambda x)\sin\frac{2n\pi}{L}}{\lambda^2+\left(\frac{2n\pi}{L}\right)^2}\right]_0^L \\
&= 2\lambda L\left[\frac{C_1\cos(\lambda L)-C_1-C_2\sin(\lambda L)}{4n^2\pi^2-\lambda^2L^2} + \frac{2C_3\sinh^2\frac{\lambda L}{2}+C_4\sinh(\lambda L)}{4n^2\pi^2+\lambda^2L^2}\right]
\end{aligned}
\tag{A2}
$$

$$
\begin{aligned}
b_{n,r} &= \frac{2}{L}\int_0^L \phi_r(x)\sin\frac{2n\pi x}{L}\mathrm{d}x = \frac{2}{L}\int_0^L (C_1\sin(\lambda x)+C_2\cos(\lambda x)+C_3\sinh(\lambda x)+C_4\cosh(\lambda x))\sin\frac{2n\pi x}{L}\mathrm{d}x \\
&= \frac{2}{L}\int_0^L C_1\sin(\lambda x)\sin\frac{2n\pi x}{L}\mathrm{d}x + \frac{2}{L}\int_0^L C_2\cos(\lambda x)\sin\frac{2n\pi \mathrm{x}}{\mathrm{L}}\mathrm{d}x + \frac{2}{L}\int_0^L C_3\sinh(\lambda x)\sin\frac{2n\pi x}{L}\mathrm{d}x \\
&\quad + \frac{2}{L}\int_0^L C_4\cosh(\lambda x)\sin\frac{2n\pi x}{L}\mathrm{d}x = \frac{2C_1}{L}\left[-\frac{\sin\left(\lambda+\frac{2n\pi}{L}\right)x}{2\left(\lambda+\frac{2n\pi}{L}\right)} + \frac{\sin\left(\lambda-\frac{2n\pi}{L}\right)x}{2\left(\lambda-\frac{2n\pi}{L}\right)}\right]_0^L \\
&\quad + \frac{2C_2}{L}\left[-\frac{\cos\left(\lambda+\frac{2n\pi}{L}\right)x}{2\left(\lambda+\frac{2n\pi}{L}\right)} + \frac{\cos\left(\lambda-\frac{2n\pi}{L}\right)x}{2\left(\lambda-\frac{2n\pi}{L}\right)}\right]_0^L + \frac{2C_3}{L}\left[\frac{\lambda\cosh(\lambda x)\sin\frac{2n\pi x}{L}}{\lambda^2+\left(\frac{2n\pi}{L}\right)^2} - \frac{\frac{2n\pi}{L}\sinh(\lambda x)\cos\frac{2n\pi x}{L}}{\lambda^2+\left(\frac{2n\pi}{L}\right)^2}\right]_0^L \\
&\quad + \frac{2C_4}{L}\left[\frac{\lambda\sinh(\lambda x)\sin\frac{2n\pi x}{L}}{\lambda^2+\left(\frac{2n\pi}{L}\right)^2} - \frac{\frac{2n\pi}{L}\cosh(\lambda x)\cos\frac{2n\pi x}{L}}{\lambda^2+\left(\frac{2n\pi}{L}\right)^2}\right]_0^L \\
&= -4n\pi\left[\frac{C_1\sin(\lambda L)+C_2\cos(\lambda L)-C_2}{4n^2\pi^2-\lambda^2L^2} + \frac{C_3\sinh(\lambda L)+2C_4\sinh^2\frac{\lambda L}{2}}{4n^2\pi^2+\lambda^2L^2}\right].
\end{aligned}
\tag{A3}
$$

Acknowledgements This study was supported by the SLDRCE Independent Research Fund of the Ministry of Science and Technology of China (Nos. SLDRCE14-B-24 and SLDRCE19-B-33).

Conflict of Interest The authors declare that they have no conflict of interest.

References

1. Wang J T S, Lin C C. Dynamic analysis of generally supported beams using Fourier series. Journal of Sound and Vibration, 1996, 196(3): 285−293
2. Naguleswaran S. Transverse vibration of an Euler–Bernoulli uniform beam on up to five resilient supports including ends. Journal of Sound and Vibration, 2002, 44: 2541−2555
3. Hozhabrossadati S M, Sani A A, Mofid M. Vibration of beam with elastically restrained ends and rotational spring-lumped rotary inertia system at mid-span. International Journal of Structural Stability and Dynamics, 2015, 15(2): 1450040
4. Yang Y B, Yau J D, Hsu L C. Vibration of simple beams due to trains moving at high speeds. Engineering Structures, 1997, 19(11): 936−944
5. Visweswara Rao G. Linear dynamics of an elastic beam under moving loads. Journal of Vibration and Acoustics, 2000, 122(3): 281−289
6. Ju S H, Lin H T. Resonance characteristics of high-speed trains passing simply supported bridges. Journal of Sound and Vibration, 2003, 267(5): 1127−1141
7. Yang Y B, Wu C M, Yau J D. Dynamic response of a horizontally curved beam subjected to vertical and horizontal moving loads. Journal of Sound and Vibration, 2001, 242(3): 519−537
8. Yang Y B, Lin C L, Yau J D, Chang D W. Mechanism of resonance and cancellation for train-induced vibrations on bridges with elastic bearings. Journal of Sound and Vibration, 2004, 269(1–2): 345–360
9. Xia H, Zhang N, Guo W W. Analysis of resonance mechanism and conditions of train-bridge system. Journal of Sound and Vibration, 2006, 297(3–5): 810–822
10. Yang Y B, Yau J D. Vertical and pitching resonance of train cars moving over a series of simple beams. Journal of Sound and Vibration, 2015, 337: 135−149
11. Sun Z. Moving-inertial-loads-induced dynamic instability for slender beams considering parametric resonances. Journal of Vibration and Acoustics, 2016, 138(1): 011014
12. Jin Z, Pei S, Li X, Qiang S. Vehicle-induced lateral vibration of railway bridges: An analytical-solution approach. Journal of Bridge Engineering, 2016, 21(2): 04015038
13. Zeng Q, Yang Y B, Dimitrakopoulos E G. Dynamic response of high speed vehicles and sustaining curved bridges under conditions of resonance. Engineering Structures, 2016, 114: 61−74
14. Yang Y B, Yau J D. Resonance of high-speed trains moving over a series of simple or continuous beams with non-ballasted tracks. Engineering Structures, 2017, 143: 295−305
15. Yang Y B, Li M, Zhang B, Wu Y T, Yang J P. Resonance and cancellation in torsional vibration of monosymmetric I-sections under moving loads. International Journal of Structural Stability and Dynamics, 2018, 18(9): 1850111
16. Yang Y B, Yau J D, Urushadze S. Wave transmission of linked railcars moving over multi simple beams under dual resonance. Journal of Sound and Vibration, 2019, 452: 51−57
17. Yang Y B, Lin C W, Yau J D. Extracting bridge frequencies from the dynamic response of a passing vehicle. Journal of Sound and Vibration, 2004, 272(3–5): 471–493
18. Gentile C, Saisi A. Continuous dynamic monitoring of a centenary iron bridge for structural modification assessment. Frontiers of Structural and Civil Engineering, 2015, 9(1): 26−41
19. Sun Z. Normal mode splitting in a moving-particles-pumped mechanical oscillator: Clamped-hinged shallow beam. Scientific Reports, 2018, 8(1): 9803
20. Wang H, Zhu Q X, Li J, Mao J X. HU S T, Zhao X X. Identification of moving train loads on railway bridge based on strain monitoring. Smart Structures and Systems, 2019, 23(3): 263−278
21. Sun Z. Frequency comb free vibration behavior of a single-span plate pumped by low-speed moving inertial loads. International Journal of Structural Stability and Dynamics, 2022, 22(7): 2250032
22. Li G H, Xiang H F, Shen Z Y, Fan L C, Shi D, Huang D Z. Bridge Structure Stability and Vibration. Beijing: China Railway Press, 1992 (in Chinese)
23. Pesterev A V, Yang B, Bergman L A, Tan C A. Revisiting the moving force problem. Journal of Sound and Vibration, 2003, 261(1): 75−91
24. Mamandi A, Kargarnovin M H, Younesian D. Nonlinear dynamics of an inclined beam subjected to a moving load. Nonlinear Dynamics, 2010, 60(3): 277−293
25. Piccardo G, Tubino F. Dynamic response of Euler–Bernoulli beams to resonant harmonic moving loads. Structural Engineering and Mechanics, 2012, 44(5): 681−704
26. Johansson C, Pacoste C, Karoumi R. Closed-form solution for the mode superposition analysis of the vibration in multi-span beam bridges caused by concentrated moving loads. Computers & Structures, 2013, 119: 85−94
27. Gašić V, Šalinić S, Obradović A, Milovančević M. Application of the lumped mass technique in dynamic analysis of a flexible L-shaped structure under moving loads. Engineering Structures, 2014, 76: 383−392
28. Tan G J, Wang W S, Jiao Y B, Wei Z G. Free vibration analysis of continuous bridge under the vehicles. Structural Engineering and Mechanics, 2017, 61(3): 335−345
29. Maximov J T, Dunchev V P. Investigation of dynamic response of "bridge girder-telpher-load" crane system due to telpher motion. Coupled Systems Mechanics, 2018, 7(4): 485−507
30. Jeong B, Kim T, Lee U. Vibration analysis of a multi-span beam subjected to a moving point force using spectral element method. Structural Engineering and Mechanics, 2018, 65(3): 263−274
31. Gong F Z, Sun Z. Computation of impact effect of multi-span beam bridge under light-rail vehicle. In: Proceedings of 2019 International Conference on Civil Engineering, Mechanics and Materials Science. Lancaster: DEStech Publications, 2019, 7–11